Cell Reports
Physical Science

CellPress
OPEN ACCESS

Article

Development of 4D-bioprinted shape-morphing magnetic constructs for cartilage regeneration using a silk fibroin-gelatin bioink

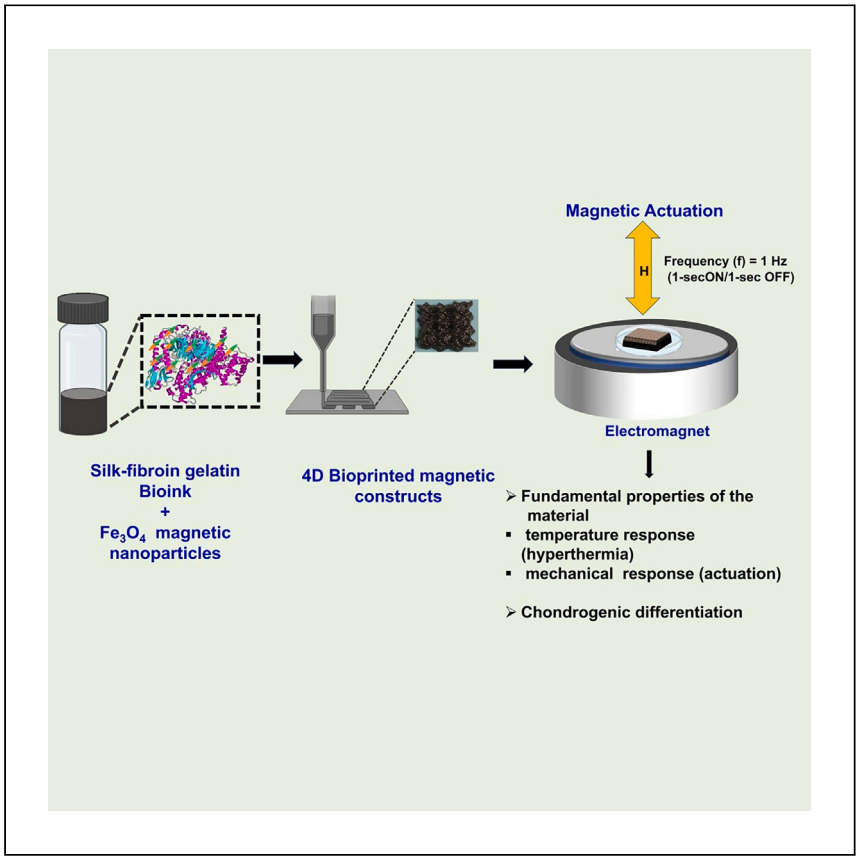

Chakraborty et al. develop a 4D-bioprinted magnetic construct using silk fibroin-gelatin bioinks for articular cartilage regeneration, encapsulated with anisotropic magnetic nanoparticles and bone-marrow-derived mesenchymal stem cells. These shape-morphing constructs exhibit thermal and mechanical responses when actuated by an external magnetic field. They also demonstrate superior chondrogenesis when actuated for a longer time (30 min vs. 5 min).

Juhi Chakraborty, Julia Fernández-Pérez, Milad Takhsha Ghahfarokhi, ..., Carlos Mota, Sourabh Ghosh, Lorenzo Moroni

sourabh.ghosh@textile.iitd.ac.in (S.G.)
l.moroni@maastrichtuniversity.nl (L.M.)

Highlights

Developed a 4D-bioprinted construct using silk fibroin-gelatin bioink

Conjugated bioink with magnetic nanoparticles for articular cartilage regeneration

Control of actuation and thermal response of the developed constructs achieved

Superior chondrogenesis attained when actuated for a longer time in a magnetic field

Chakraborty et al., Cell Reports Physical Science 5, 101819
March 20, 2024
https://doi.org/10.1016/j.xcrp.2024.101819

Please cite this article in press as: Chakraborty et al., Development of 4D-bioprinted shape-morphing magnetic constructs for cartilage regeneration using a silk fibroin-gelatin bioink, Cell Reports Physical Science (2024), https://doi.org/10.1016/j.xcrp.2024.101819

Cell Reports
Physical Science

CellPress
OPEN ACCESS

Article

Development of 4D-bioprinted shape-morphing magnetic constructs for cartilage regeneration using a silk fibroin-gelatin bioink

Juhi Chakraborty,[1,2] Julia Fernández-Pérez,[2] Milad Takhsha Ghahfarokhi,[3] Kenny A. van Kampen,[2] Tim ten Brink,[2] Jopeth Ramis,[2] Maria Kalogeropoulou,[2] Riccardo Cabassi,[3] César de Julián Fernández,[3] Franca Albertini,[3] Carlos Mota,[2] Sourabh Ghosh,[1,*] and Lorenzo Moroni[2,4,*]

SUMMARY

External magnetic fields can regulate cellular responses when interacting with magnetic nanoparticles (MNPs). Here, we develop a 4D-bioprinted construct by incorporating anisotropic MNPs into a silk fibroin-gelatin bioink with human bone-marrow-derived mesenchymal stromal cells for cartilage regeneration. We measure the magnetic-field-induced temperature response of the acellular construct, determine its mechanical response (actuation), and compare it with the MNPs. Constructs are then magnetically actuated, and their effects on chondrogenesis are investigated. Actuation is induced cyclically every other day (5 min and 30 min/day) for 21 days. Actuation for 30 min exhibits enhanced early (Sox-9 and aggrecan) and late (collagen-II) expression with downregulation of hypertrophic markers (collagen-X and matrix metalloproteinase-13) and enhanced matrix deposition, total collagen, and glycosaminoglycan compared to the constructs actuated for 5 min, kept static, or with no MNPs. Hence, magnetic field actuation could be a significant strategy to stimulate constructs mechanically for articular cartilage regeneration.

INTRODUCTION

The unmet clinical need for articular cartilage regeneration inflicts a massive burden on the healthcare system and the global economy.[1] Since the intrinsic healing potential of articular cartilage is limited, cartilage damage frequently results in osteoarthritis.[2] Various strategies have been developed to improve the regenerative potential of articular cartilage.[3–5] For instance, both human embryonic stem cells and adult stem cells have been used, together with chondrogenic soluble substances, to gain insight into how polymeric scaffold compliance directs chondrogenic tissue regeneration.[6] Although 3D bioprinting with suitable bioinks has the potential for organ repair and tissue regeneration,[7–9] bioinks are constrained by poor tailorability, limited responsiveness, and weak actuation properties.[10] As a result, there is an increasing focus on developing hydrogels with programmable physicochemical features, on-demand controllability, and responsiveness. When exposed to extrinsic triggers (pH, light, magnetic [or electric] field, and temperature), stimuli-responsive hydrogels can distinctly alter their chemical and/or physical properties.[11]

Magnetic hydrogels (ferrogels) responsive to an external magnetic field are produced when magnetic nanoparticles (MNPs) are incorporated into a polymer network.[12]

[1]Department of Textile and Fibre Engineering, Indian Institute of Technology Delhi, New Delhi 110016, India

[2]Department of Complex Tissue Regeneration, MERLN Institute for Technology-Inspired Regenerative Medicine, Maastricht University, 6229 ER Maastricht, the Netherlands

[3]Institute of Materials for Electronics and Magnetism (IMEM), National Research Council (CNR), Parco Area delle Scienze 37/A, 43124 Parma, Italy

[4]Lead contact

*Correspondence: sourabh.ghosh@textile.iitd.ac.in (S.G.), l.moroni@maastrichtuniversity.nl (L.M.)

https://doi.org/10.1016/j.xcrp.2024.101819

Ferrogels have several benefits over conventional stimuli-responsive polymers, including actuation capability by a non-contact force such as a magnetic field. This distinct attribute diversifies the application of magnetic hydrogels in drug delivery,[13,14] soft robotics,[15] tissue engineering,[16,17] and environmental engineering.[18,19] Magnetic-responsive hydrogels are developed by combining hydrogel networks with magnetic-responsive additives, which make them different from those stimulus-responsive hydrogels whose responsive features originate from the intrinsic property of the material. As a result, the magnetically actuated hydrogels deform, move, and transform under the influence of the magnetic stimuli in a remote and controllable way.[12] Additionally, the magnetic actuating feature can be combined with other stimulus-responsive hydrogels to generate multiple responsiveness, which can fulfill many requirements of practical biomedical tasks and broaden the scope of applications for magnetic hydrogels.[12] One of those stimuli is magnetic hyperthermia, which locally induces thermic energy in the cells when the magnetic particles are exposed to an external magnetic field. The generated heat can be exploited in cancer cell therapy, drug release, and activation of the cells' heat-sensitive receptors.[20,21] In addition, it has been shown that moderate temperatures generated by magnetic hyperthermia contribute to better cell differentiation.[22,23] It has been documented that the generated heat may enhance mitochondrial activity and facilitate the expression of specific genes.[24] Although the exact mechanisms related to these effects are still to be further elucidated, such pieces of evidence can aid in the enhancement of various cellular functions, such as proliferation, adhesion, and differentiation.[21] Hyperthermia has also been thought of as an alternative treatment in clinical applications for tissue regeneration.[25]

Various patterning methods have recently been established to develop hydrogel objects with intricate architecture. Additive manufacturing (AM) has gained intense popularity in fabrication methods due to its ability for instant fabrication of intricate 3D architectures with biomaterials of different nature starting from computer-aided designs.[26,27] Among AM technologies, extrusion-based bioprinting can drive the spatially defined dispersion of bioactive materials and cell types within the construct; such a pattern can also permit or require a spatially defined stimulation. AM methods that can modify physical properties and trigger a structural response in the materials using contactless stimuli such as magnetic force, pH, ions, and temperature are typically called 4D printing.[11,28] This technique has been enforced in the field of tissue engineering that enables the fabrication of complex, functional biological constructs by including time as a fourth dimension in conventional 3D bioprinting technologies. These 4D-bioprinted constructs could change in shape or function over time by utilizing a variety of stimuli-responsive biomaterials and 4D bioprinting techniques.[28] Interestingly, adding MNPs improves the controllability and resolution of 4D-printed hydrogel constructs. For instance, Chen et al.[29] fabricated a hydrogel octopus that could be actuated by a programmed external magnetic field and locomote alternately from left to right using 3D printing and magneto-responsive nanocomposite. Kim et al.[30] established a method for 4D printing of soft materials with programmed ferromagnetic domains that enable quick and reversible shape changes when applying a magnetic field. The biocompatibility of the nanoparticles makes iron-oxide-based actuation devices beneficial for further investigation as remotely triggered 4D-bioprinted constructs.[31] Although anisotropic ferromagnetic nanoparticles have been reported previously, they involve dangerous synthesis steps with the production of goethite, transformation into hematite, and further reduction to magnetite under an H_2 atmosphere.[32] In light of this, we previously[33] demonstrated a novel two-step synthetic process for fabricating anisotropic MNPs that starts with hematite and does not require hydrogen gas. Noteworthy, human mesenchymal stem cells (hMSCs) could internalize the

MNPs when they were directly administered to cells at high doses of up to 5 mg/mL. Additionally, the MNPs displayed minimal toxicity at lower and more practical concentrations. Further, when integrated into poly(caprolactone-co-trimethylcarbonate) urethane acrylate and printed via digital light processing into a rigid shape, their alignment could be tuned along with the magnetic field.[33] Depending on the direction of the field, the MNPs exhibited distinctive attraction or repulsion, suggesting that their alignment could be adjusted with the magnetic field. The ability of cells embedded in constructs to differentiate into osteogenic[34,35] or chondrogenic[36,37] tissue is known to be enhanced by mechanical stimulation. Although we have demonstrated the potential of the synthesized anisotropic MNPs in actuating nanocomposites with defined movements,[33] it is appealing to determine whether these anisotropic MNPs would cause human bone-marrow-derived mesenchymal stromal cells (BM-MSCs) encapsulated in an appropriate bioink to undergo differentiation when actuated by a magnetic field.

In extrusion-based bioprinting, the bioinks' rheological properties determine their printability and shape fidelity. Silk fibroin-gelatin (SF-G) has demonstrated outstanding rheological properties[38,39] and has been shown to be an excellent biomaterial[40] for cartilage development.[41,42] When cultured in 3D-bioprinted SF-G constructs, BM-MSCs downregulate hypertrophic differentiation and undergo articular cartilage differentiation.[43] SF-G has been demonstrated to play a crucial role in intrinsically regulating the Wnt/β-catenin pathway in primary chondrocytes and mesenchymal progenitor cells.[43,44] Karahaliloğlu et al. fabricated magnetic SF electrically mediated hydrogel (e-gel) constructs by an electrogelation process using 8% of concentrated *Bombyx mori* SF aqueous solution as a novel sort of bone-graft substitute.[45] The findings showed that introducing MNPs enhanced the mechanical characteristics of SF e-gel constructs, including increased hydrophilicity. Although MNP-loaded e-gel scaffolds from SF and from other magnetic hydrogels[46,47] have demonstrated their potential for the treatment of bone defects or other pathologies, mechanical simulation of SF-G constructs by an external stimuli to improve the cell-regeneration process remains unexplored. In the present study, we fabricated a 4D-bioprinted shape-morphing construct by incorporating our previously synthesized novel anisotropic MNPs[33] into an SF-G bioink. The bioink was crosslinked via mushroom tyrosinase and *in vitro* primed with human BM-MSCs with the aim of improving the chondrogenic potential of the BM-MSCs when the constructs are actuated magnetically. The fundamental properties of the bioprinted constructs and their response to the external magnetic field were precisely characterized by advanced techniques and models. We also analyzed the effect of applying a programmed magnetic actuation on the chondrogenic differentiation of the bioprinted constructs via gene expression and extracellular matrix (ECM) formation.

RESULTS

Rheological characterization

Extensive rheological measurements of the SF-G acellular bioinks have been studied previously.[39,48] Dynamic rheological measurements were carried out for the SF-G blends with different concentrations of the MNPs to evaluate the effects of MNP concentration on the rheological behavior of the samples. Both the storage (G') and loss modulus (G'') were studied for SF blends with 0, 0.5, 5, and 50 mg/mL MNPs with respect to the applied frequency (frequency sweep) and the applied strain (strain sweep).

The frequency sweep measurements of the four SF blends (Figure 1A) depicted that the G' values were significantly higher than G'' values, designating an accurate gel-like material. Both the G' and G'' values increased upon increasing the concentration of the MNPs,

Please cite this article in press as: Chakraborty et al., Development of 4D-bioprinted shape-morphing magnetic constructs for cartilage regeneration using a silk fibroin-gelatin bioink, Cell Reports Physical Science (2024), https://doi.org/10.1016/j.xcrp.2024.101819

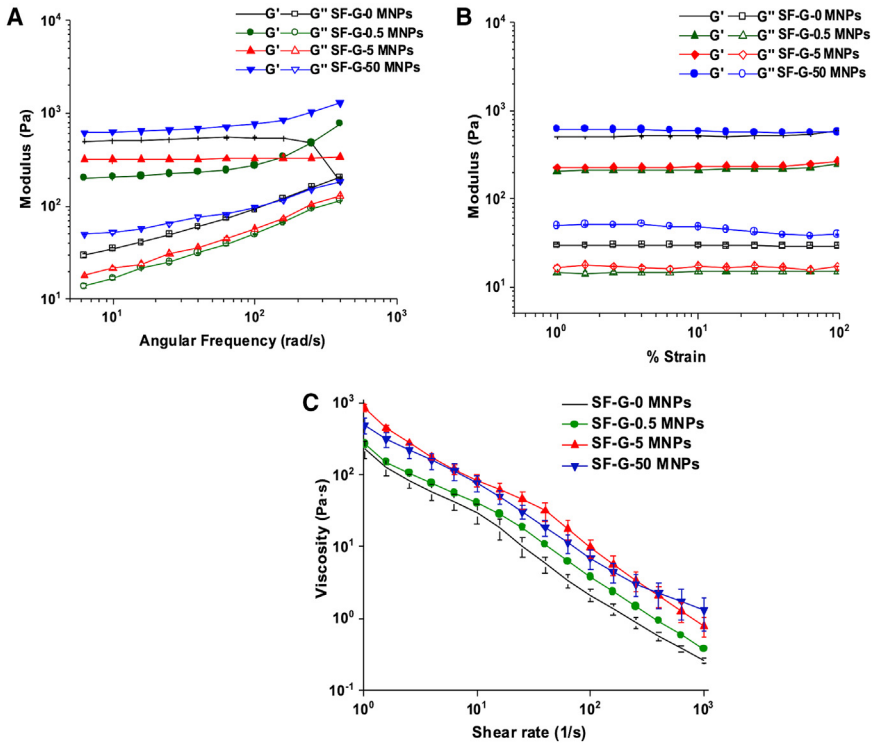

Figure 1. Rheological analysis of the silk fibroin-gelatin (SF-G) acellular bioink with varying magnetic nanoparticle concentrations

(A) Frequency sweep and (B) amplitude sweep test results showing the variation of the dynamic storage modulus (*G′*) and loss modulus (*G″*); (C) flow behavior analysis. SF-G, silk fibroin-gelatin, where 0, 0.5, 5, and 50 represent the concentration of magnetic nanoparticles (MNPs) in mg/mL. Data are presented as means ± SD, n = 3.

except for the control (SF-G-0 MNPs). However, a crossover point was observed at a specific frequency in the SF-G-0 MNPs, which specifies a drop in the elastic character in the gel system. One possible explanation for this is that the fiber network might have lost its integrity at a higher frequency, and the gel matrices have broken into smaller units. When 0.5 mg/mL was added to the control ink, i.e., SF-G-0 MNPs, no significant difference compared to the control ink formulation could be observed. Yet, when the concentration was increased to 10 and 100 times, i.e., 5 and 50 mg/mL of the MNPs, an increase in the modulus was seen. The loss factor (tan δ), or G''/G', which establishes the relative elasticity of viscoelastic materials, has been also calculated. Acellular bioinks with a tan(δ) value of less than 0.1 are classified as stiff gels and show well-ordered systems. Tan(δ) values were 0.24 ± 0.023 for the control acellular bioink (SF-G-0 MNPs), 0.16 ± 0.005 for SF-G-0.5 MNPs, 0.11 ± 0.011 for SF-G-5 MNPs, and 0.13 ± 0.006 for SF-G-50 MNPs. This demonstrated that the MNP-containing acellular bioinks had higher storage modulus and better-ordered gel microstructures than the control bioink.

Oscillatory strain sweep tests were carried out to determine a linear viscoelastic region, where the moduli (*G′* and *G″*) were independent of the applied strain up to a critical deformation. Further, strain sweep tests were executed from 0.1% to 1,000% strain amplitude at 1 Hz and 25°C static frequency. All the SF-G blends had a higher *G′* value than *G″* value (Figure 1B), indicating that an elastic gel had been formed.

The flow behavior of the SF blends was determined for various concentrations of MNPs in a range of shear rates from 1 to 1,000 s^{-1} (Figure 1C). All the blends of SF with different MNP concentrations exhibited shear-thinning behavior at 25°C.

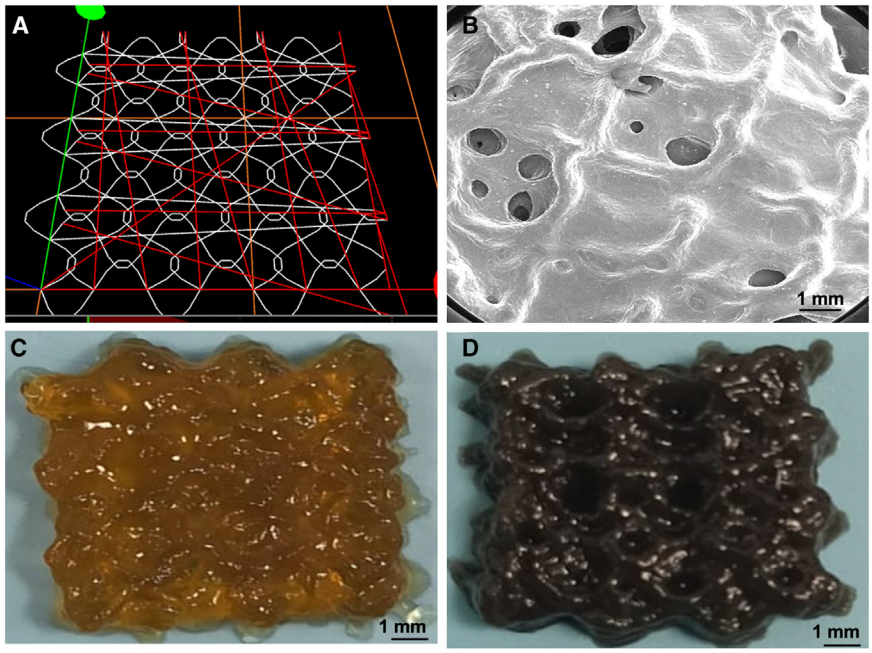

Figure 2. Morphological analysis of the acellular constructs

(A) The final bioprinting pathway designed by a G-code simulator.

(B) Field-emission SEM image depicting the sinusoidal morphology of the construct.

(C and D) Optical images of the 4D-bioprinted constructs (C) without magnetic nanoparticles (MNPs) as control and (D) with MNPs (5 mg/mL).

This was evident by a distinct decline in the viscosity as the shear rate increased, indicating a power-law decay region. The viscosity increased upon increasing the MNP concentration, except for the SF-G-5 MNPs sample, whose viscosity was almost twice (845.08 Pa s) that of the sample with the highest MNP concentration (484.56 Pa s) at a shear rate of 1 s^{-1}. However, a decline in viscosity was observed at a shear rate above 100 s^{-1} compared to SF-G-50 MNPs. The shear-thinning behavior enables the systematic flow of the acellular bioink across the fine nozzles; simultaneously, quick recovery due to increased viscosity results in high shape fidelity.[49]

Morphology of the constructs

The final bioprinting pathway designed by a G-code simulator is shown in Figure 2A. The surface morphology of the acellular bioprinted construct and its morphological features were determined using scanning electron microscopy (SEM) analysis (Figure 2B). The sinusoidal pattern of the printed construct is visible. The designed pores are clearly defined, with no cracks or other defects. The calculated spreading ratio of the constructs was 1.065 $\pm$ 0.08. The optical images of the constructs without MNPs (control) and with MNPs (~5 mg/mL) are displayed in Figures 2C and 2D, respectively.

Magnetic characterizations: Quantification of the thermal and actuation response in a magnetic field

The magnetization of the construct was measured along different directions with respect to the plane of the construct (Figure 3A). All these loops overlap, showing an isotropic distribution of the MNPs in the construct. The detailed characteristics of the loops are provided in Table S3. The M_r/M_{max} ratio showed the same value measured for the powder MNPs (0.12), whereas the H_c value (13 mT) was slightly larger. We have recently reported the magnetic properties of these MNPs.[33]

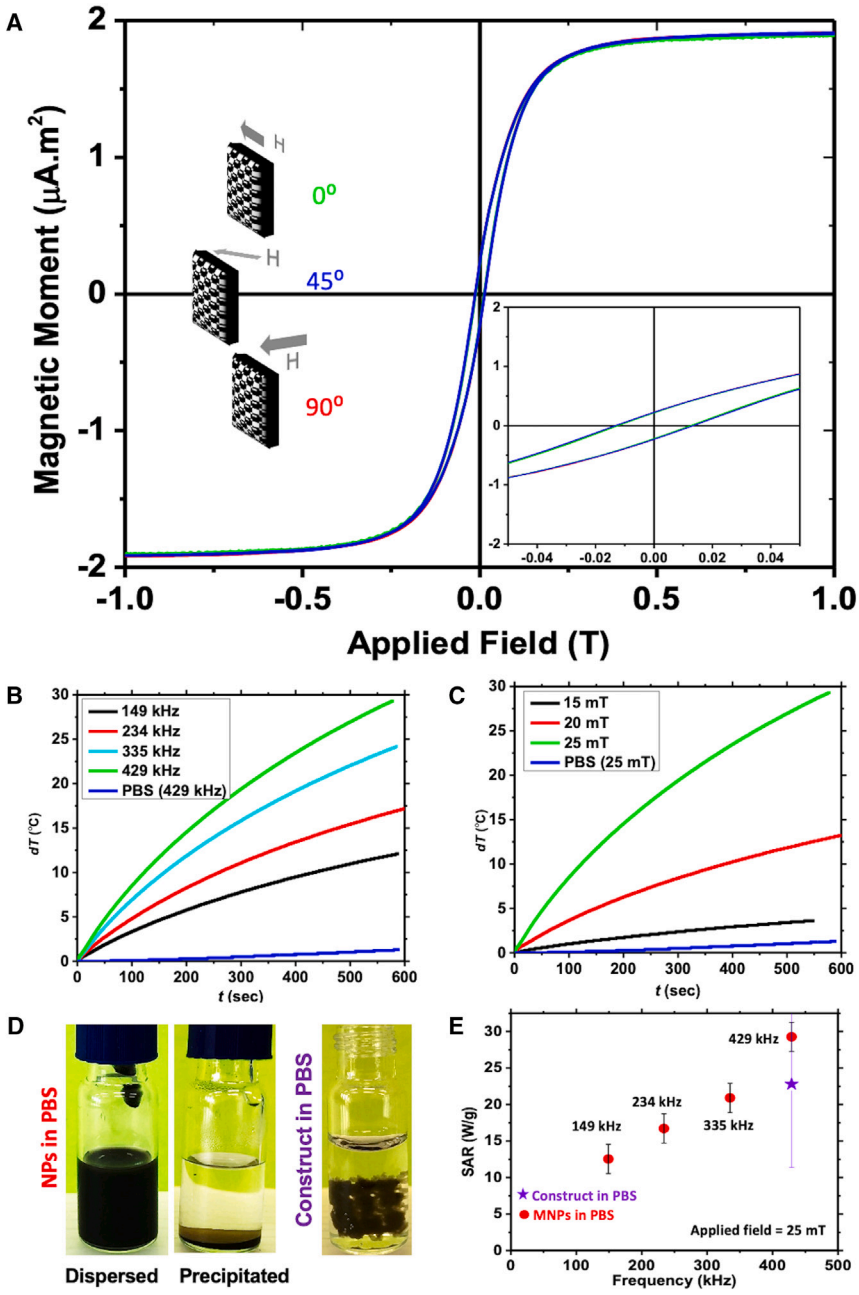

Figure 3. Quantification of the thermal response of the acellular construct in a magnetic field

(A) Magnetization curves vs. magnetic fields at room temperature applying magnetic fields along 0°, 45°, and 90° with respect to the construct's plane (uncertainty ≈5%). The inset graph shows the magnetization curves in the range of $\mu_0 H$ = 50 mT.

(B) The sample's temperature increase in PBS was measured by applying $|\mu_0 H|$ = 25 mT and different frequencies from 149 to 429 kHz.

(C) The sample's temperature increase in PBS was measured by applying the magnetic field at a fixed frequency of 429 kHz and different magnetic field strength $|\mu_0 H|$ = 15–25 mT.

(D) Images of the samples prepared for the hyperthermia tests showing the dispersed and precipitated magnetic nanoparticles (MNPs) in PBS (20 mg/mL) and a printed construct in 1 mL of PBS.

(E) SAR values for MNPs in PBS at $|\mu_0 H|$ = 25 mT as a function of frequency. The SAR value obtained for the construct in PBS at $|\mu_0 H|$ = 25 mT, f = 429 kHz is also plotted as a purple star.

Concerning the particle dimensions and shape (around 178 nm in length and 55 nm in width), the particles were mainly magnetically blocked, confirmed by the small hysteresis loop,[33] similarly for the constructs. Therefore, we are dealing with magnetically isotropic constructs with magnetic properties similar to those of the powder MNPs.

The magnetic hyperthermia experiments for the MNPs dispersed in phosphate-buffered saline (PBS) were recorded at a fixed magnetic field. Different frequencies are shown in Figure 3B, while fixed frequency and variable magnetic field strength is presented in Figure 3C. In all the experimental conditions, an increase of temperature was observed that reached up to around $\Delta T \approx 30^{\circ}C$ at 25 mT and 429 kHz after 600 s. The experiment performed with the construct in this last condition confirms that the construct can be heated using alternating magnetic field (AMF), but the increase was only $\Delta T \approx 0.4^{\circ}C$. This significant difference between the heat efficiency of the construct and the powders can be related, for instance, to the small amount of MNPs (around 0.55 mg) in the construct. We have investigated this difference by calculating the specific absorption rate (SAR). However, to evaluate this magnitude it was necessary to consider that the measurements were not recorded in a perfect adiabatic condition, i.e., some heat dissipated over time toward the external environment. In addition, it was necessary to consider that the hyperthermia measurements were performed for the precipitated powders, i.e., the heat emission was not uniform in space and time, similarly for the construct (Figure 3D). We have developed a thermodynamic model of the time-dependent temperature evolution that considers both effects (described in detail in the supplemental information). Figure 3E presents the SAR of the powders in PBS under different frequencies together with the SAR value of the construct. The SAR of the construct and the corresponding value of MNPs were almost similar, showing only approximately 17% of difference.

We also explored the induced remotely controlled actuation of the construct using an optical setup (Figure S2) that allows detecting even tiny displacements through the position of the reflected beam when the magnetic field is changed. Figures 4A and 4B show the beam's position starting from magnetic field zero and |0.588| T, respectively. Figure 4C shows the evolution of the laser position displacement and the corresponding bending angle. The bending angle was calculated based on elementary geometry, as described in detail in the supplemental information. Videos S1 and S2 show the deformation of the sample when applying pulses of the applied magnetic field, switching the direction of the field alternatively. The construct showed a quasi-linear bending actuation when both the positive and negative magnetic fields were applied (average linear fit $R^2 \approx 0.98$). No considerable difference was observed in the bending actuation behavior of the construct when ramping up, ramping down, or switching the sign of the magnetic field. The deformations showed that the construct always bends toward the same magnetic pole regardless of the sign of the applied magnetic field. Considering magnetic force equations in bending cantilevers (for details see supplemental information), the applied maximum magnetic force to the construct was calculated to be around 0.1 mN, which has given rise to the maximum bending angle of around 1.59° at $\mu_0 H = +0.78$ T. Further elaborations on magnetic properties of the particles and the construct, and related quantification of the thermal response in a magnetic field, are presented in Note S1.

Analysis of gene expression enhancement by magnetic field actuation

The chondrogenic ability of the bioprinted constructs that were magnetically actuated was evaluated by RT-PCR at early (day 7) and late (day 21) stages of chondrogenic culture (Figure 5). Constructs actuated for 30 min exhibited an upregulation

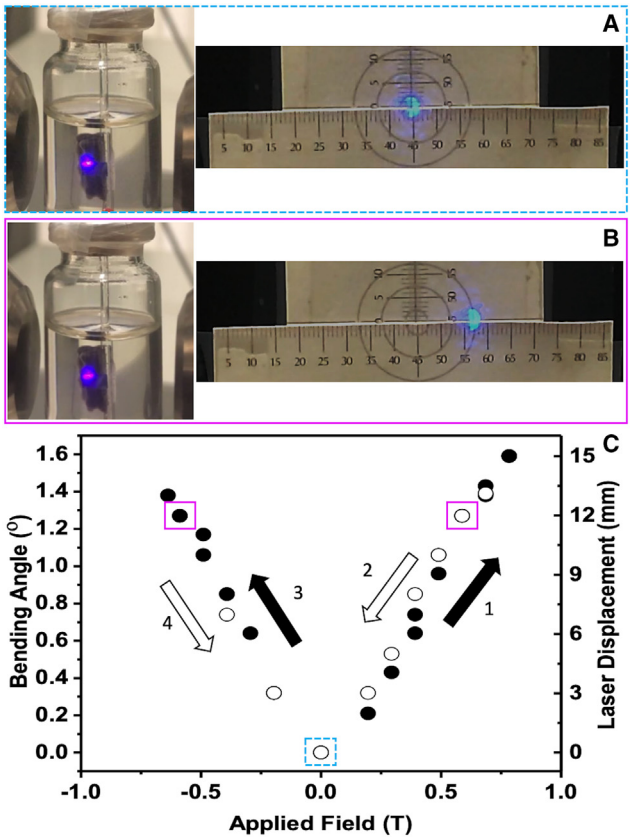

Figure 4. Quantification of the actuation response of the acellular construct in a magnetic field

(A) The construct status and the laser spot's position on the screen at $\mu_0 H = 0$ T.

(B) The construct status and the laser spot's position on the screen at $|\mu_0 H| = 0.588$ T.

(C) Bending deformation of the construct vs. the applied magnetic field (uncertainty ≈0.1°). The solid circles show the deformation when the field is increased, and the open circles show the deformation of the construct when the field is reduced. The sequence of the experiment is also shown by arrows. The positions of (A) and (B) are highlighted.

for the chondrogenic markers, i.e., Col 2A1 (15-fold), ACAN (12-fold), and SOX 9 (16-fold) on day 21 compared to the control ($p < 0.0001$). Interestingly, the expression levels were higher than those in the other experimental groups. Notably, the relative expression of the bioprinted constructs actuated for 5 min was similar to that of the control on days 7 and 21, specifically around 6- to 6.3-fold for Col 2A1, 8- to 8.29-fold in ACAN, and 10.5- to 12-fold in SOX 9 on day 21. The static constructs showed the lowest expression of the chondrogenic markers Col 2A1 (3.1-fold), ACAN (6-fold), and SOX 9 (7-fold) on day 21.

When assessed for the hypertrophy markers Col 10A1 and matrix metalloproteinase-13 (MMP 13), a decline in expression was observed on day 21 for the constructs actuated for 30 min. The decrease in the expression level was less than 2-fold in both Col 10A1 and MMP 13 ($p < 0.0001$). Although only a nominal change was observed in the expression levels of the static constructs on day 21 compared to day 7, it was found to be non-significant. On the other hand, Col 1A1 exhibited almost similar expression levels on day 7 (4.69-fold) and day 21 (4.5-fold) in the static samples. At the same time, constructs actuated for 30 min showed a decreasing trend on day 21 compared to day 7 ($p < 0.0001$).

Cell Reports
Physical Science
Article

CellPress
OPEN ACCESS

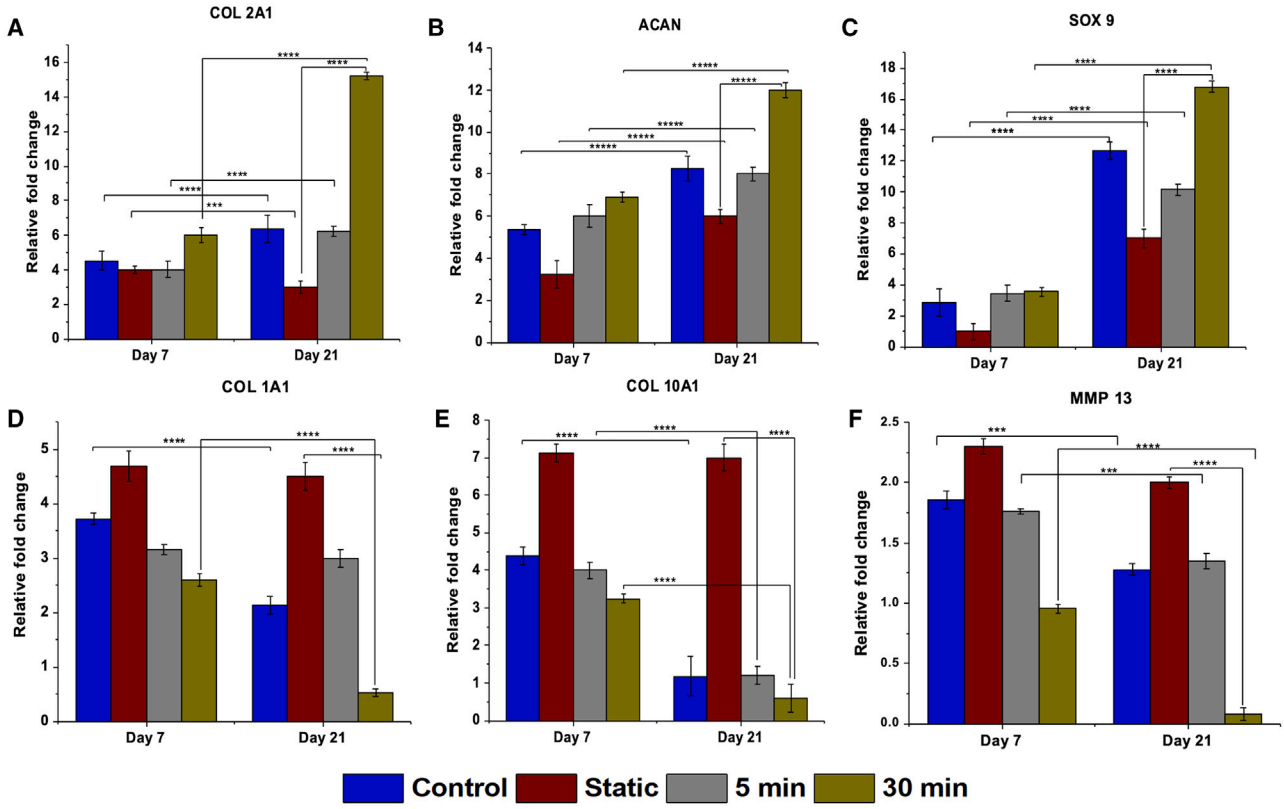

Figure 5. Relative gene expression analysis of the bioprinted constructs for the set of chondrogenic differentiation-, dedifferentiation-, and hypertrophy-specific markers

Chondrogenic markers (A) Col 2A1, (B) ACAN, and (C) SOX 9, dedifferentiation marker (D) Col 1A1, and hypertrophy markers (E) Col 10A1 and (F) MMP 13 on days 7 and 21, significant at *$p < 0.05$, **$p < 0.01$, ***$p < 0.001$, and ****$p < 0.0001$. Data are presented as means ± SD. Control: silk fibroin-gelatin (SF-G) only, i.e., the construct without MNPs. Static: magnetic constructs maintained in an incubator at a static condition. 5 min: magnetic constructs actuated for 5 min. 30 min: magnetic constructs actuated for 30 min.

Assessment of cell proliferation and ECM production enhancement by magnetic field actuation

DNA content estimation was carried out on days 7 and 21 to determine the proliferation of the human BM-MSCs encapsulated within the different sets of the bioprinted constructs (Figure 6A). A decline in the DNA content was observed on day 21 in all the sets of the bioprinted constructs. However, on days 7 and 21, maximal DNA content was noticed in the constructs with 30 min of actuation. This was followed by the control, constructs actuated for 5 min, and the static one.

Sulfated glycosaminoglycans (GAGs) were analyzed to determine the cartilaginous matrix's chondrogenic differentiation and temporal accumulation. Accumulated GAGs increased on day 21 in the control constructs and those actuated for 5 min and 30 min (Figure 6B). At the same time, the constructs in static condition exhibited decreased GAG production on day 21 compared to day 7. The highest expression was observed with the constructs with 30 min of actuation on day 21.

The total collagen content was estimated to determine the extent of ECM formation by the encapsulated human BM-MSCs within the bioprinted constructs on day 7 and day 21 (Figure 6C). The highest collagen content was observed on day 21 in 30-min actuated constructs. The control samples and the constructs actuated for 5 min showed similar behavior. The static samples exhibited a decline in collagen content

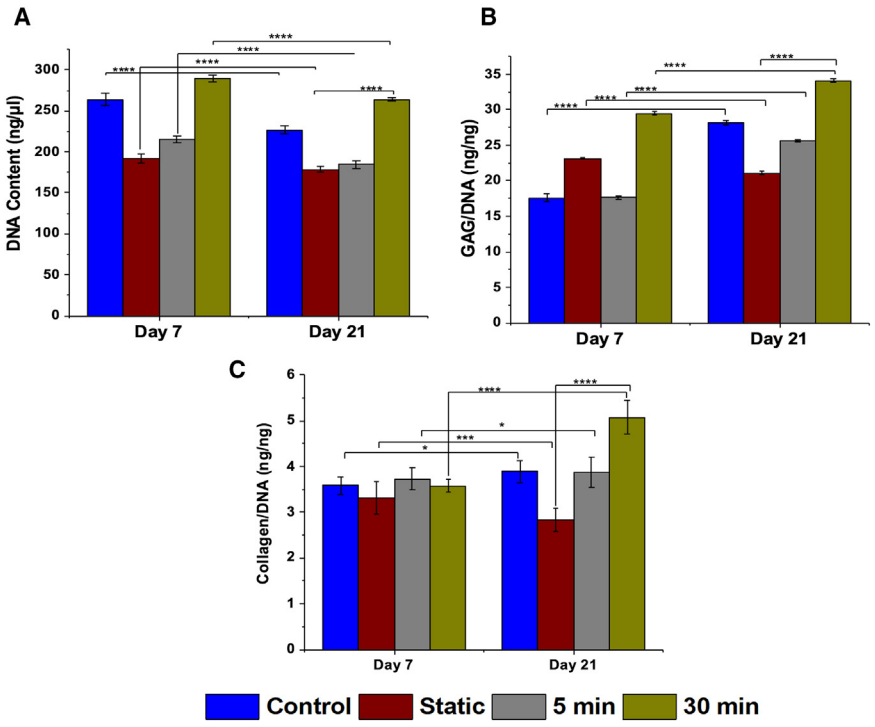

Figure 6. Biochemical analysis of the bioprinted constructs on days 7 and 21

(A) The total DNA content (ng/µL), (B) glycosaminoglycan (GAG) content normalized to the DNA content (ng/ng), and (C) collagen content normalized to the DNA content (ng/ng). Significant at ****$p < 0.0001$; data are presented as means ± SD. Control: silk fibroin-gelatin (SF-G) only, i.e., the construct without MNPs. Static: magnetic constructs maintained in an incubator at a static condition. 5 min: magnetic constructs actuated for 5 min. 30 min: magnetic constructs actuated for 30 min.

on day 21. Interestingly, GAG and collagen estimation normalized to DNA showed a declining trend with the bioprinted constructs in static condition. In contrast, an increasing trend was observed with all the sets of constructs on day 21.

DISCUSSION

Magnetic fields are effective in stimulating cellular behavior and cell migration, proliferation, and differentiation to cure diseases and repair damaged tissues.[50,51] For fabrication of polymers or dynamic structures that respond to magnetic stimuli, some recent publications documented the earliest attempts to integrate cells with magnetic cues in biomaterial inks or bioprinted hydrogel scaffolds.[52,53] Some studies have also established the role of MNP-conjugated magnetic constructs, including foams and nanofibers, in promoting cellular proliferation as well as osteogenic[50,54] and chondrogenic[16] differentiation of cells, including MSCs. Del Bianco et al.[55] reported the incorporation of iron oxide superparamagnetic nanoparticles into SF films for potential use as a bioactive coating in regenerative medicine. In another study, Chouhan et al.[56] developed a magnetically responsive matrix based on SF by embedding magnetic iron oxide nanoparticles within silk nanofibers and actuating it by their in-house-developed magnetic actuator device. Although these studies demonstrated the potential of magnetically decorated silk for biomedical applications, no bioprinting use has been reported to date for cellular regeneration by magnetic actuation. It has been demonstrated that the use of external magnetic fields has positive benefits on articular cartilage regeneration.[16] Our study attempts to exploit the stimulatory potential of the magnetic field toward chondrogenic function and the regeneration of articular cartilage. Hence, we hypothesized that

amalgamating magnetically decorated constructs with magnetic actuation might create synergistic microenvironments favorable for articular cartilage regeneration. In brief, we have developed 4D-bioprinted magnetic constructs using SF-G bioinks, which enhanced the chondrogenic differentiation of BM-MSCs post printing by spatially adjusted mechanical stimulation of the encapsulated cells.

The *G′* value of the magnetic hydrogel, i.e., SF-G with our previously[33] synthesized MNPs, was higher than that of the non-magnetic counterpart. Hence, the incorporation of MNPs acted as reinforcement to the mechanical structure of the polymeric matrix. Moreover, the modulus findings show that when MNP concentration was increased there was a greater degree of intermolecular crosslinking, which enhanced the storage modulus and stiffened the gel. As a result, the development of stronger gels showed good MNP dispersion and confirmed a well-ordered microstructure and gel network. This increase is caused by the reinforcing impact of the inorganic MNPs, which serve as extra crosslinkers to aid in creating gels. Similarly, Agrawal et al.[57] discovered that when the quantity of laponite particles was increased, the *G′* value of PLA-PEO-PLA gel increased significantly, indicating the development of new connections by the nanoparticles. Based on the reports from flow behavior and lactate dehydrogenase assay[33] with these MNPs, 5 mg/mL of the MNPs was chosen for bioprinting and all experiments. To have a complete view of the complex construct-cell interaction, an inclusive characterization of the material is required. We have precisely characterized the fundamental properties of our bioprinted constructs and their response to external magnetic fields with advanced techniques and models. To the best of our knowledge, this is the first report that has comprehensively traced multiple responses (heat, actuation) of the biomagnetic materials in an external magnetic field, filling the gap in the literature in this respect. Generation of heat by MNPs in an AMF is due to power loss typically governed by three mechanisms: (1) viscous damping due to particle motion (Brown relaxation); (2) magnetic moment reorientation in the MNPs (Néel relaxation); and (3) magnetic hysteresis loss due to magnetization reversal.[58,59] Maximum SAR was obtained when choosing the highest applied magnetic field intensity (25 mT) and frequency (429 kHz) on the instrument. This combination of field and frequency is still far below the critical value for the H-*f* patient tolerance reported by Atkinson et al. ($\sim 6 \times 10^5$ mT s^{-1}).[60] Therefore, the SAR value can be increased if needed by selecting higher magnetic fields and frequencies. We exclude the contribution of Néel relaxation in generating heat because the average particle size (around 178 nm length and 55 nm width) is well above the typical threshold sizes (30–40 nm), below which Néel relaxation process is dominant, as the MNPs are superparamagnetic.[60] Brown relaxation may also be considered to be due to the particles' large size. In this mechanism, the free rotation of the magnetized particles produces heat.[60] This mechanism could be present in the MNPs in a dispersion, but the MNPs in the construct are trapped in the polymer matrix during the printing and crosslinking process. This could significantly reduce the contribution of Brown relaxation in the generation of heat. We have evidenced this phenomenon by comparing the hyperthermia properties of the MNPs dispersed in PBS and in a more viscous dispersant such as isopropanol (IPA). In fact, at 20°C the viscosity of IPA is 2.37 mPa s, whereas that of PBS is similar to water (1 mPa s).[61] We observed the effect of the viscosity on the mobility of the particles in the slower precipitation of the particles dispersed in IPA, as shown in Figure S1B. The obtained SAR values of MNPs in IPA were reduced with respect to those in PBS by around 32% in 15 mT and around 50% in 20 mT (Figure S1E and Table S2), confirming the reduction of heat-generation capacity by the increase of viscosity of the dispersant. Hence, we exclude that both Néel and Brown relaxation mechanisms give rise to heat generation in the printed construct.

Please cite this article in press as: Chakraborty et al., Development of 4D-bioprinted shape-morphing magnetic constructs for cartilage regeneration using a silk fibroin-gelatin bioink, Cell Reports Physical Science (2024), https://doi.org/10.1016/j.xcrp.2024.101819

Considering the observation of open hysteresis loops (Figure 3A), we identified the hysteresis losses as the main source of heating in the constructs. It is worth mentioning that the temperature increase of the construct through this mechanism is highly dependent on various characteristics of the applied magnetic field such as magnetic field frequency. Therefore, we can reasonably neglect the heating effect of the constructs in our magnetic actuation tests because the frequency of the magnetic fields applied in those tests are orders of magnitude lower than in the hyperthermia test.

Deformation of the construct in a magnetic field could be summarized by the fact that a magnetic object moves toward areas where the magnetic field lines are denser. Practically, the sample cannot be placed precisely in the middle having equal distances with respect to the magnetic poles. The closer pole attracts the magnetized sample when the field is switched on. The reason why the construct always moved toward the same magnetic pole even when the magnetic field direction was switched (by changing the sign of the fields) is the small coercive field of the MNPs (Figure 3A). Therefore, upon applying the magnetic field, the magnetic components of the magnetized sample switch so that the construct always bends toward the nearest electromagnetic pole.

We also tried to align MNPs in a crystal bond and measured the orientation dependence of M/H at room temperature (Figure S4). The hysteresis loops showed that a certain orientation effect is induced, which is coherent with the results we have reported recently.[33] However, the H_c and M_r values did not vary in our experiments. This may reflect the polymagnetic domain behavior of the MNPs. Understanding the external magnetic field response mechanism of such multidomain complex systems would require extensive magnetic simulations.

RT-PCR analysis gave insight into the differentiation status of BM-MSCs in the bioprinted constructs. For the constructs actuated for 30 min, upregulation of Col 2A1 and SOX 9 was noticeably higher (15- and 17-fold, respectively). In contrast, the expression of these markers occurred much later and at lower levels in the other groups. SOX 9 is considered an early chondrogenic marker and is vital in early chondrogenesis.[62] ACAN, the main cartilage proteoglycan, was likewise strongly expressed in the constructs with 30-min actuation. The lower expression of ACAN (5-fold) on the static bioprinted construct indicates that although less chondrogenesis was observed, as ascertained from the Col 2A1 expression, upon detection of Col 1A1, we cannot exclude the possibility of the formation of fibrocartilage on the static samples. Lower levels of Col 10A1 and MMP 13 expression in the 30-min actuated samples indicates that the actuation of the magnetic constructs for a longer time can intercept or retard the differentiation of the BM-MSCs into hypertrophic phenotype. This is quite interesting, given that most long-term *in vitro* cultures frequently cause hypertrophy and restrict the utilization of BM-MSCs as a cell source for cartilage repair.[63] It is worth mentioning that we have used an SF-G bioink for our study, which intrinsically plays a key role in regulating the Wnt/β-catenin and transforming growth factor β (TGF-β) Indian Hedgehog signaling pathways. This is crucial, since these signaling cascades play an essential role in cell proliferation, cell migration, and chondrocyte differentiation.[42] Further, SF allows for cell adhesion, cell proliferation, and surface chemistry for a range of cell types, including stem cells, and it has the potential to function as a supportive matrix.[64] This bioink aided in abating hypertrophy during the development of a 3D-bioprinted cartilage.[38,42] Several other studies have also established the potential role of SF-G in cartilage regeneration both *in vitro* and *in vivo*.[65,66] However, the application of a

fourth dimension by the inclusion of MNPs in SF-G makes our study stand out from these already reported ones. The gene expression patterns found in this study generally share several similarities with the chondrogenic process seen after mesenchymal condensation during *in vivo* limb development. However, it is worth bearing in mind that we studied chondrogenesis for 21 days in culture. Culturing them for over a month would give us a better perspective of the entire process.

We observed a decline in proliferation within the chondrogenic culture medium in all conditions, which can be due to cellular differentiation.[42] Many studies have validated this by indicating that the BM-MSCs' proliferation rate decreased with an increase in differentiation.[67] Upon actuation for a longer time (30 min), the cells in the constructs secreted a more cartilage-specific matrix. Reduced cell proliferation combined with enhanced GAG and collagen production in constructs actuated for 30 min was mainly related to their differentiation state and increased matrix formation. Overall, the findings presented here demonstrate how the microenvironment around the vital cartilage matrix proteins affects both their transcription and subsequent synthesis of the ECM. Furthermore, the magnetic actuation of the bioprinted constructs for a long time modulates the cellular activities of the encapsulated cells.

The main targeted application of the magnetically decorated SF-G constructs toward the development of the magnetically deformable constructs (Video S3) lies in the mechanical stimulation of cells, specifically toward articular cartilage development. The bioink composed of SF-G and MNPs worked synergistically in promoting BM-MSC adherence and differentiation upon magnetic actuation. Huang et al.[68] showed that Fe_3O_4 nanoparticles improved the growth of human MSCs owing to their potential to minimize intracellular H_2O_2 via intrinsic peroxidase-like activity. Additionally, they proposed that Fe_3O_4 nanoparticles might expedite cell-cycle progression.[68] Compared to the study by Huang et al., the novelty of our work lies in the fact that the inclusion of MNPs within the SF-G bioink not only resulted in shape-morphing constructs via magnetic actuation, but also improved the differentiation ability of BM-MSCs. Upon addition of MNPs into the constructs in large quantity, the microenvironment inside or on the surface of the bioprinted constructs is composed of numerous small magnetic fields. Hence, the overall effect is expected to be strengthened. As a result, the amplified action may impact ion channels on cell membranes and influence cytoskeletal architecture when the bioprinted constructs are exposed to the external magnetic field.[69,70]

Future studies should aim at further exploring different architectures of the bioprinted constructs and time of exposure. We have selected a specific sinusoidal fiber pattern to maintain stimulation as homogeneously as possible across the biological constructs. Changing the strand thickness or the sinusoidal amplitude is expected to result in a different stress-strain field on the encapsulated cells, which would further impinge on their differentiation. Changing the architecture into more fractal-like patterns would also enable the study of more heterogeneous mechanical stimulation, which could provide additional avenues for stem cell-based regeneration of interface tissues. We have chosen conservatively to study short times of exposure (i.e., 5 and 30 min), but further studies could be aimed at identifying more thoroughly the time of stimulation regime that could further enhance stem cell chondrogenic differentiation. Here, we have reasonably excluded the magnetic-field-induced effect of heat in molecular characterization by referring to the frequency of the applied magnetic field and the mechanism of the hyperthermia effect. We have highlighted the magnetic-field-induced actuation as the sole effect responsible for the observed enhancement of the cell activity. Therefore, the BM-MSCs exhibited decreased proliferation and started chondrogenic differentiation in the

constructs actuated for 30 min compared to those actuated for a shorter time (5 min). From the obtained results, the presence of MNPs and longer magnetic actuation time resulted in better chondrogenesis.

Functional MNP-based magnetic systems offer a variety of new applications, from tissue engineering to cellular control. A promising strategy for understanding cell-function control is magnetic mediation. Using MNP-based actuation to manipulate cellular shape and function is a relatively recent technique that has shown great promise in tissue engineering. In the present study, we developed 4D-bioprinted magnetic constructs by incorporating MNPs into an SF-G bioink encapsulated with BM-MSCs. The fundamental properties of the bioprinted constructs and their response upon magnetic actuation were precisely characterized by advanced techniques and models. The magnetic actuation test showed a linear deformation response of the constructs as a function of the magnetic field. The applied maximum magnetic force to the construct was calculated to be approximately 0.1 mN, which gave rise to the maximum bending angle of around 1.59° at $\mu_0 H$ = +0.78 T.

The constructs were then magnetically actuated using a compatible setup, and the effects of actuation on chondrogenesis were investigated. Magnetic actuation for a longer time (30 min) with the cyclic application of magnetic field (on/off pattern) at the frequency of 1 Hz exhibited better articular cartilage chondrogenesis compared to that for a shorter time (5 min). This has been ascertained from the upregulated gene expression with the chondrogenic markers Col 2A1, ACAN, and SOX 9 and reduced expression of the hypertrophic markers Col 10A1 and MMP 13, accompanied by a correspondent increase in GAG and collagen content. At the same time, the magnetic constructs kept under static conditions hindered chondrogenesis. Hence, these 4D-printed constructs hold potential regarding articular cartilage chondrogenesis.

EXPERIMENTAL PROCEDURES

Resource availability

Lead contact

Further information and requests for resources and reagents should be directed to and will be fulfilled by the lead contact, Professor Lorenzo Moroni (l.moroni@maastrichtuniversity.nl).

Materials availability

This study did not generate new unique reagents.

The Central Silk Technological Research Institute (Central Silk Board), Bangalore, Ministry of Textiles, Government of India, kindly provided the *Bombyx mori* cocoons. All other reagents utilized in the study are described in detail, along with the experimental methods.

Data and code availability

All the necessary data have been provided in the main text and supplemental information. Any additional data related to this paper can be obtained from the lead contact upon reasonable request. This study did not generate/analyze datasets or code.

Cell culture and expansion

The Institute for Regenerative Medicine at Texas A&M Health Science Center provided the human BM-MSCs (donor d8011L, female, age 22).[71] The cells were expanded at a density of 5,000 cells/cm^2 in a proliferation medium composed of minimum essential medium alpha (α-MEM) supplemented with Glutamax (Gibco, USA) and 10% fetal

Please cite this article in press as: Chakraborty et al., Development of 4D-bioprinted shape-morphing magnetic constructs for cartilage regeneration using a silk fibroin-gelatin bioink, Cell Reports Physical Science (2024), https://doi.org/10.1016/j.xcrp.2024.101819

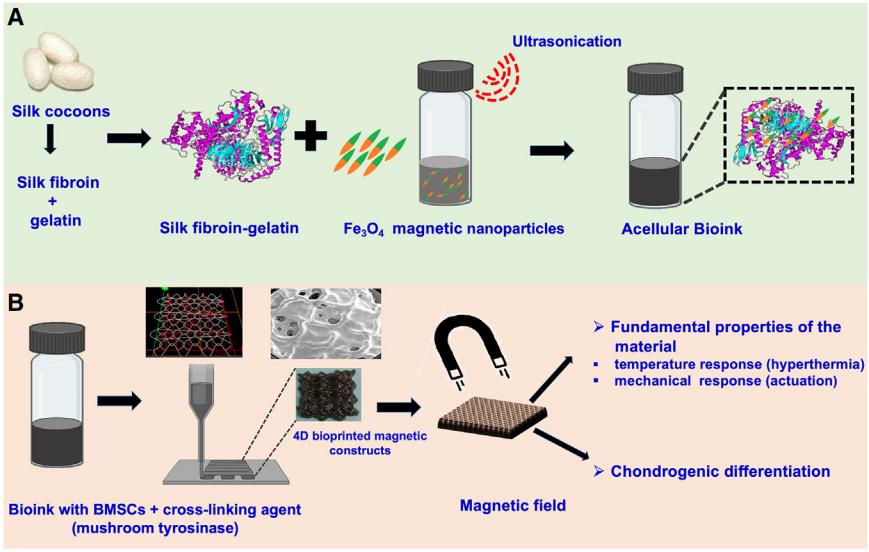

Figure 7. Illustration of the steps involved in the development of a 4D-bioprinted construct for articular cartilage regeneration

(A) Preparation of the magnetically decorated silk fibroin-gelatin bioink with 5 mg/mL magnetic nanoparticles.

(B) Fabrication of the 4D-bioprinted constructs, magnetic field stimulation, fundamental magnetic characterization of the material, and molecular characterization for chondrogenic differentiation.

bovine serum (FBS) (Sigma-Aldrich), 37.5 μg/mL ascorbic acid (Sigma-Aldrich), and 100 U/mL penicillin-streptomycin (Gibco), in an environment that was adequately humidified at 37°C and 5% CO_2. The cells between passages 3 and 4 were used for all the experiments. The subculture was carried out at 80% confluence.

Preparation of the bioink

We used the procedure outlined elsewhere[72] to extract the SF solution from *Bombyx mori* cocoons. For the acellular bioink, the SF-G blend was obtained by dissolving 8% of the gelatin from porcine skin type A (Sigma-Aldrich) in autoclaved 5% SF solution. In brief, to 800 μL of the SF solution, 80 mg of the gelatin was added, and the resulting mixture was then incubated at 37°C for 30 min. The prepared SF-G blend was combined with 100 μL of media supplement (10× α-MEM, Gibco) and 10% FBS to produce the control ink.

The synthesized MNPs[33] were purified several times with deionized water and dried at 110°C. Eventually, 5 mg of the MNP was ultrasonicated (Bandelin electronic ultrasonicator) for 5 min in 500 μL of PBS. The volume of the resultant magnetic solution was then adjusted with the control ink to form 5 mg/mL of the MNP-containing acellular bioink. The cell-encapsulated bioink was prepared by adding 1×10^7 cells/mL to the control ink (SF-G) and SF-G-MNP ink separately. Mushroom tyrosinase (800 units/mL; Sigma-Aldrich) was added to the bioink before printing to initiate cross-linking, with the aim of improving the chondrogenic potential of the BM-MSCs when the constructs were actuated magnetically (Figure 7).

Rheological analysis of the acellular bioink

Rheological measurements were carried out using a DHR-2 rheometer (TA Instruments) furnished with a solvent trap and Peltier heating element. A 20-mm cone-plate geometry was used with an angle of 2.002° for *in situ* gelation and all consecutive measurements. All measurements were performed at 25°C, corresponding to the gelation temperature of silk. The acellular bioinks were freshly prepared and used

Table 1. Composition of various acellular bioinks

Sample ID	Silk fibroin (SF, %)	Gelatin (G, %)	MNPs (mg/mL)
SF-G-0 MNPs	5	8	0
SF-G-0.5 MNPs	5	8	0.5
SF-G-5 MNPs	5	8	5
SF-G-50 MNPs	5	8	50

directly for the experiments. The samples are reported in Table 1. The rheometer was immediately loaded with 84 μL of the sample to study the impact of shear on various inks at 25°C. The flow behavior (pre-crosslinking) was assessed in the shear rate range of 0.1–1,000 s^{-1}.

All of the blends' dynamic storage (G') and loss modulus (G'') were determined in oscillatory mode at 25°C post crosslinking using mushroom tyrosinase. By maintaining the frequency constant at 1 Hz during the amplitude sweep measurement, the materials were examined for strain values ranging from 0.1% to 1,000%. Further, the prepared inks were analyzed using a frequency sweep measurement with a frequency range of 10–1,000 rad s^{-1} while maintaining a constant strain of 1%.

Fabrication of the 4D-bioprinted constructs

A custom-written code in Python (version 3.7.0; Python Software Foundation) was generated to create the pathway for the extruder. Using the sinusoidal function, the Y coordinate was calculated (Equations 1 and 2). Thereafter, cutoff values were set to mark the construct's boundaries.

$$Y(x) = A\sin(\omega x + \varphi) \quad \text{(Equation 1)}$$

$$Y(x) = A\sin(-\omega x + \varphi) \quad \text{(Equation 2)}$$

For this study, A, ω, and φ were kept at a constant value of 100, 22, and 0, respectively. A is amplitude of the sine wave, ω is angular frequency of the sine wave, x is the x coordinate of the printed path, and φ is phase difference.

A sterile 3-mL syringe with a pneumatic piston was gently loaded with the human BM-MSCs-laden SF-G and SF-G-MNP bioink. Air bubbles in the syringe were removed before the bioink could gel and then mounted into the bioprinter's (BioScaffolder 3.1, GeSiM, Germany) pressure-based direct dispensing printhead. All the constructs were printed using a microcapillary nozzle with a diameter of 200 μm (Nordson EFD Tapered Tip, 27 gauge), a pressure of 65 ± 20 kPa, and a speed of 3,000 mm s^{-1}. The final 4D-bioprinted construct was 10 mm × 10 mm in length and width, 1.75 mm in height, and composed of seven layers. To produce a suitable initial degree of reticulation, the printing was done 20 min after adding mushroom tyrosinase.

Before transferring into the non-adherent 6-well plate (Thermo Fisher Scientific), the printed constructs were held at room temperature for approximately 20–30 min. The cells encapsulated within the constructs were first allowed to expand in the cell-proliferation medium for 48 h before being switched to the chondrogenic medium for chondrogenic differentiation. DMEM/F12 (Gibco) supplemented with Glutamax, 1% 100× ITS (insulin-transferrin-selenium) liquid media supplement, 40 μg/mL proline (Sigma-Aldrich), 0.1 μM dexamethasone (Sigma-Aldrich), 37.5 μg/mL ascorbic acid (Sigma-Aldrich), 100 U/mL penicillin-streptomycin (Gibco), and 10 ng/mL TGF-β1 (PeproTech) made up the chondrogenic medium. The 4D bioprinted

constructs were maintained in the chondrogenic differentiation medium until day 21. The medium was changed every other day.

Field-emission scanning electron microscopy imaging

The acellular printed constructs were air-dried after the dehydration in ethanol. Samples were then gold-sputtered using an EMITECH K550X (UK) sputter coater and were imaged using a JEOL JSM-7500F (JEOL, Japan) field-emission scanning electron microscope.

Magnetic measurements: Quantification of the thermal and actuation response in a magnetic field

Magnetic hysteresis loops of the construct were measured as a function of an external magnetic field up to $|\mu_0 H|$ = 1 T at room temperature by an alternating gradient force magnetometer (MicroMag 2900). We applied the magnetic field with respect to different directions of the construct's plane: along the edges, 45° inclined concerning the constructs plane, and perpendicular to the constructs plane. The sample was measured in a quasi-dehydrated condition (Figure S1A).

Magnetic hyperthermia measurements under AMF were performed by an AC applicator (DM100; nanoScale Biomagnetics, Zaragoza, Spain). The measure consists of recording the temperature increase of the sample dispersion over time in an AMF. The device allows performing measurements in quasi-adiabatic conditions, and the frequency and strength of the applied field can be selected between 149 and 429 kHz and between 15 and 25 mT, respectively. An optical-fiber sensor measures the temperature variation in a 1-mL PBS dispersion containing 20 mg of the MNPs. Measurements were also performed using 1 mL of IPA as a dispersant to investigate the influence of the viscosity of the dispersant on the hyperthermia properties. Table S1 shows the different viscosity of PBS and IPA upon increasing the temperature from 20°C to 50°C. Hyperthermia measurements were performed on a construct immersed in 1 mL of PBS in the applied frequency f = 429 kHz and the magnetic field $|\mu_0 H|$ = 25 mT. The MNPs in one construct were estimated to be approximately 0.55 mg.

The SAR at a specific frequency and strength of the magnetic field is calculated through the following formula:

$$\mathrm{SAR} = \frac{C}{m} \times \frac{\mathrm{dT}}{\mathrm{dt}}, \qquad \text{(Equation 3)}$$

where C is the specific heat capacity of the dispersant per unit volume ($C_{PBS} \approx c_{water} \approx$ 4,179.6 J/kL, $C_{IPA} \approx$ 2,106.48 J/kL), m is the concentration of the sample ($mg_{iron\ oxide}$/mL) and $\frac{dT}{dt}$ is the initial slope of the temperature curves after 5, 10, 20, and 30 s depending on the slope of the obtained curves. In all cases, the measurements were performed from a stabilized thermal condition of the sample at approximately 21°C.

The deformation of the construct induced by an external magnetic field was investigated by an in-house-built optical setup. A piece of a silicon wafer was mounted on the fronting free edge of the construct. This wafer acts as a laser beam mirror. The opposite side of the construct was glued to a capillary tube from the edge in a flag-fashion shape (Figure S2). The flag was immersed and fixed in a transparent glass bottle containing PBS. The bottle was placed between the poles of an electromagnet capable of applying reversible magnetic fields up to 1 T in the position of the sample. One laser beam was focused on the sample wafer, and the reflected beam was observed on a screen. The deformation of the construct induced by the magnetic field produces a change in

Please cite this article in press as: Chakraborty et al., Development of 4D-bioprinted shape-morphing magnetic constructs for cartilage regeneration using a silk fibroin-gelatin bioink, Cell Reports Physical Science (2024), https://doi.org/10.1016/j.xcrp.2024.101819

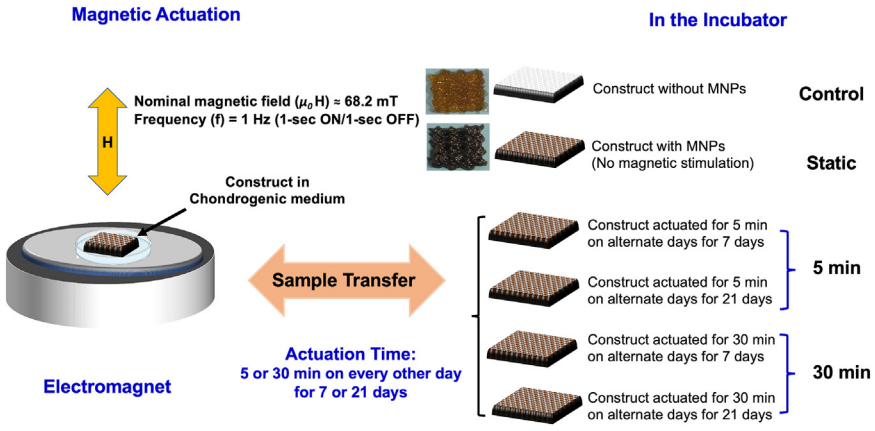

Figure 8. Schematic representation showing magnetic field actuation of the bioprinted constructs and the entire sample set for molecular characterization

the reflection beam, observed in the displacement of the laser spot on the screen. Details of the setup are described in Figures S2 and S3.

Magnetic field actuation of the bioprinted constructs for molecular characterization

The constructs were magnetically actuated by an electromagnet (1,900 N, 12 V DC, Conrad) applying a cyclic ON/OFF magnetic field of $\mu_0 H \approx 68.2$ mT to induce actuation with a frequency of 1 Hz. For the purpose of magnetic field actuation, the constructs were taken out of the incubator for 5 min or 30 min every other day (for maximum 7 or 21 days). In addition, two samples were always kept in the incubator through the entire experiment: the constructs without the MNPs that served as a control and the sample that were kept at a static condition with no magnet field actuation. In total, four groups were examined: control—SF-G only, i.e., the construct without MNPs, static-magnetic constructs maintained in an incubator at a static condition, 5-min magnetic constructs actuated for 5 min, and 30-min magnetic constructs actuated for 30 min. The overall process of magnetic actuation is depicted in a schematic form in Figure 8.

Gene expression analysis

The bioprinted constructs were collected on days 7 and 21. The constructs from all the groups and the control set were digested with 250 μg/mL Protease XIV enzyme (Sigma) for 20 min at 37°C to isolate the embedded cells.[43,73] Centrifugation at 1,200 rpm separated the cells from the gel debris. According to the manufacturer's instructions, total RNA was extracted using the RNeasy Minikit with on-column DNase treatment (Qiagen). RNA quantity and quality were assessed using a BioDrop μLITE+ (BioDrop, Cambridge, UK). Following the manufacturer's instructions, cDNA was synthesized utilizing at least 100 ng of total RNA employing the Bio-Rad iScript cDNA synthesis kit in a 20-μL reaction. Due to the low concentration of cDNA recovered from the constructs, SSO Advanced PreAmp Supermix (Bio-Rad) was used for the pre-amplification stage. For quantitative PCR (qPCR), 10 μL of iQ SYBR Green Supermix (Bio-Rad), 0.2 μM forward and reverse primers (Table 2), 3 ng of cDNA, and diethyl pyrocarbonate-treated water were employed. An equivalent volume of DNase- and RNase-free water was used for no-RT controls. The samples were incubated for 3 min at 95°C in a CFX96 IVD Real-Time PCR system (Bio-Rad), and 39 cycles of 15 s at 95°C and 30 s at 58°C thermocycling were performed. GAPDH was used as a housekeeping gene. The $2^{-\Delta\Delta Ct}$ technique was

Table 2. List of genes analyzed using RT-qPCR

Gene name	Full name	Forward primer 5′-3′	Reverse primer 3′-5′
GAPDH	glyceraldehyde-3-phosphate dehydrogenase	ATG GGG AAG GTG AAG GTC G	TAA AAG CAG CCC TGG TGA CC
Col 1A1	collagen type I alpha 1 chain	AGG GCC AAG ACG AAG ACA TC	AGA TCA CGT CAT CGC ACA ACA
Col 2A1	collagen type II alpha 1 chain	GGC AAT AGC AGG TTC ACG TAC A	CGA TAA CAG TCT TGC CCC ACT T
Col 10A1	collagen type X alpha 1 chain	GAC TCC CTC CTC ACT GTC GC	AGG GAA GTC TCC CTC ACT TGT
ACAN	aggrecan	AGG CAG CGT GAT CCT TAC C	GGC CTC TCC AGT CTC ATT CTC
SOX 9	SRY-box transcription factor 9	TTC CGC GAC GTG GAC AT	TCA AAC TCG TTG ACA TCG AAG GT
MMP 13	matrix metalloproteinase-13	CCA GAC TTC ACG ATG GCA TTG	GGC ATC TCC TCC ATA ATT TGG C

used to determine relative gene expression. Monolayer human BM-MSCs at day 0 (cultured without chondrogenic factors) were used as a comparator or control.

Estimation of DNA, glycosaminoglycan, and total collagen content

For DNA quantification, the constructs were collected on days 7 and 21, put in Eppendorf tubes, snap-chilled immediately in liquid nitrogen, and kept at −80°C until further analysis. The constructs were then thawed at room temperature. Proteinase K treatment was used for the digestion of the ECM. Samples were kept in 1.5-mL Eppendorf tubes and treated for 16 h at 56°C with 250 mL of 50 mM Tris/1 mM EDTA/1 mM iodoacetamide solution containing 1 mg/mL proteinase K solution. After digestion, the samples were freeze-thawed thrice in liquid N_2 to aid DNA extraction. DNA content was assessed using a CyQuant cell-proliferation assay kit (Thermo Fisher). In brief, samples were lysed in a lysis buffer containing RNase A for 1 h at room temperature to degrade the cellular RNA. A 96-well plate was filled with 100 μL of each sample (done in triplicate) and 100 μL of 2× GR-dye solution, after which the mixture was allowed to sit for 15 min at room temperature. DNA standard solution was used to prepare a standard curve, and fluorescence intensity was measured at 520 nm, the emission wavelength (excitation wavelength of 480 nm).

Proteinase K digestion steps were further employed to measure GAG content using a 1,9-dimethylmethylene blue zinc chloride double salt (DMMB; Sigma-Aldrich) solution (16 mg/L DMMB). In brief, the absorbance difference at 525 and 595 nm was determined after 150 μL of DMMB solution was combined with 25 μL of sample and 5 μL of 2.3 M NaCl on a well plate with a transparent bottom. The acquired standard curve from shark-cartilage-derived chondroitin sulfate was used to compare the data.[74]

The total collagen content of the bioprinted constructs was calculated using the hydroxyproline assay.[75] Proteinase K-treated samples underwent 18 h of hydrolysis in 12 M HCl at 120°C. The material was then dried for 48 h at 55°C under a chemical safety cabinet. The dried mass was reconstituted in H_2O. One hundred microliters of chloramine T/oxidation buffer mixture was added to each sample and standard, then incubated at room temperature for 20 min. One hundred microliters of the diluted dimethylaminobenzaldehyde reagent was added to each sample and standard, then incubated for 20 min at 60°C. The absorbance was measured at 560 nm. The readings were corrected by subtracting the blank value. The amount of hydroxyproline in the samples was determined based on the standard curve. The data were adjusted to reflect the dry weight of the construct before digestion. According to the reports,[75] collagen contains 13% hydroxyproline or

a ratio of 1:7.69 between hydroxyproline and collagen, based on which the estimation of the collagen content was carried out.

Statistical analysis

All data were analyzed using one-way ANOVA and Bonferroni's multiple comparison tests. The data were reported as mean ± SD with n indicating the number of different experiments. The differences were considered significant at $p \leq 0.05$ (*), $p \leq 0.01$ (**), $p \leq 0.001$ (***), and $p \leq 0.0001$ (****). GraphPad Prism 5.01 (GraphPad, San Diego, CA, USA) was utilized for the statistical analysis.

SUPPLEMENTAL INFORMATION

Supplemental information can be found online at https://doi.org/10.1016/j.xcrp.2024.101819.

ACKNOWLEDGMENTS

J.C. is grateful to the Department of Science and Technology, India, for the Inspire Fellowship no. IF160365. We are also grateful to ZonMw (project number 11630095101) for funding. This work is also part of the project 3D-MENTOR (with project number 18647) of the VICI Research Program, financed by the Dutch Research Council (NWO).

AUTHOR CONTRIBUTIONS

J.C.: methodology, conceptualization, investigation, writing—review & editing. J.F.-P.: methodology, writing—review & editing. M.T.: methodology, writing—review & editing. K.A.v.K.: methodology, writing—review & editing. T.t.B.: methodology. J.R.: methodology. M.K.: methodology. R.C., C.d.J.F., and F.A.: review. C.M.: writing—review & editing, funding acquisition. S.G.: supervision, writing—review & editing, project administration, conceptualization. L.M.: supervision, writing—review & editing, project administration, conceptualization, funding acquisition.

DECLARATION OF INTERESTS

The authors declare no competing interests.

Received: September 23, 2023
Revised: November 23, 2023
Accepted: January 17, 2024
Published: February 6, 2024

REFERENCES

1. Widuchowski, W., Widuchowski, J., and Trzaska, T. (2007). Articular cartilage defects: study of 25,124 knee arthroscopies. Knee *14*, 177–182. https://doi.org/10.1016/j.knee.2007.02.001.

2. Huey, D.J., Hu, J.C., and Athanasiou, K.A. (2012). Unlike bone, cartilage regeneration remains elusive. Science *338*, 917–921. https://doi.org/10.1126/science.1222454.

3. Zhang, C., Cai, Y.Z., Lin, X.J., and Wang, Y. (2020). Magnetically Actuated Manipulation and Its Applications for Cartilage Defects: Characteristics and Advanced Therapeutic Strategies. Front. Cell Dev. Biol. *8*, 526. https://doi.org/10.3389/fcell.2020.00526.

4. Chawla, S., Desando, G., Gabusi, E., Sharma, A., Trucco, D., Chakraborty, J., Manferdini, C., Petretta, M., Lisignoli, G., and Ghosh, S. (2021). The effect of silk–gelatin bioink and TGF-β3 on mesenchymal stromal cells in 3D bioprinted chondrogenic constructs: A proteomic study. J. Mater. Res. *36*, 4051–4067. https://doi.org/10.1557/s43578-021-00230-5.

5. Wang, S., Luo, B., Bai, B., Wang, Q., Chen, H., Tan, X., Tang, Z., Shen, S., Zhou, H., You, Z., et al. (2023). 3D Printed Chondrogenic Functionalized PGS Bioactive Scaffold for Cartilage Regeneration. Adv. Healthc. Mater. *12*, 2301006. https://doi.org/10.1002/adhm.202301006.

6. Ghosh, S., Laha, M., Mondal, S., Sengupta, S., and Kaplan, D.L. (2009). In vitro model of mesenchymal condensation during chondrogenic development. Biomaterials *30*, 6530–6540. https://doi.org/10.1016/j.biomaterials.2009.08.019.

7. Chakraborty, J., Chawla, S., and Ghosh, S. (2022). Developmental biology-inspired tissue engineering by combining organoids and 3D bioprinting. Curr. Opin. Biotechnol. *78*, 102832. https://doi.org/10.1016/j.copbio.2022.102832.

8. Ding, Y.-W., Zhang, X.-W., Mi, C.-H., Qi, X.-Y., Zhou, J., and Wei, D.-X. (2023). Recent advances in hyaluronic acid-based hydrogels for 3D bioprinting in tissue engineering applications. Smart Materials in Medicine *4*, 59–68. https://doi.org/10.1016/j.smaim.2022.07.003.

9. Xuan, H., Hu, H., Geng, C., Song, J., Shen, Y., Lei, D., Guan, Q., Zhao, S., and You, Z. (2020). Biofunctionalized chondrogenic

shape-memory ternary scaffolds for efficient cell-free cartilage regeneration. Acta Biomater. *105*, 97–110. https://doi.org/10.1016/j.actbio.2020.01.015.

10. Morgan, F.L.C., Moroni, L., and Baker, M.B. (2020). Dynamic Bioinks to Advance Bioprinting. Adv. Healthc. Mater. *9*, 1901798. https://doi.org/10.1002/adhm.201901798.

11. Lui, Y.S., Sow, W.T., Tan, L.P., Wu, Y., Lai, Y., and Li, H. (2019). 4D printing and stimuli-responsive materials in biomedical aspects. Acta Biomater. *92*, 19–36. https://doi.org/10.1016/j.actbio.2019.05.005.

12. Li, Z., Li, Y., Chen, C., and Cheng, Y. (2021). Magnetic-responsive hydrogels: From strategic design to biomedical applications. J. Control. Release *335*, 541–556. https://doi.org/10.1016/j.jconrel.2021.06.003.

13. Xie, W., Gao, Q., Guo, Z., Wang, D., Gao, F., Wang, X., Wei, Y., and Zhao, L. (2017). Injectable and Self-Healing Thermosensitive Magnetic Hydrogel for Asynchronous Control Release of Doxorubicin and Docetaxel to Treat Triple-Negative Breast Cancer. ACS Appl. Mater. Interfaces *9*, 33660–33673. https://doi.org/10.1021/acsami.7b10699.

14. Noh, M., Choi, Y.H., An, Y.-H., Tahk, D., Cho, S., Yoon, J.W., Jeon, N.L., Park, T.H., Kim, J., and Hwang, N.S. (2019). Magnetic Nanoparticle-Embedded Hydrogel Sheet with a Groove Pattern for Wound Healing Application. ACS Biomater. Sci. Eng. *5*, 3909–3921. https://doi.org/10.1021/acsbiomaterials.8b01307.

15. Tang, J., Yin, Q., Qiao, Y., and Wang, T. (2019). Shape Morphing of Hydrogels in Alternating Magnetic Field. ACS Appl. Mater. Interfaces *11*, 21194–21200. https://doi.org/10.1021/acsami.9b05742.

16. Huang, J., Liang, Y., Huang, Z., Zhao, P., Liang, Q., Liu, Y., Duan, L., Liu, W., Zhu, F., Bian, L., et al. (2019). Magnetic Enhancement of Chondrogenic Differentiation of Mesenchymal Stem Cells. ACS Biomater. Sci. Eng. *5*, 2200–2207. https://doi.org/10.1021/acsbiomaterials.9b00025.

17. Huang, J., Liang, Y., Jia, Z., Chen, J., Duan, L., Liu, W., Zhu, F., Liang, Q., Zhu, W., You, W., et al. (2018). Development of Magnetic Nanocomposite Hydrogel with Potential Cartilage Tissue Engineering. ACS Omega *3*, 6182–6189. https://doi.org/10.1021/acsomega.8b00291.

18. Zheng, X., Wu, D., Su, T., Bao, S., Liao, C., and Wang, Q. (2014). Magnetic Nanocomposite Hydrogel Prepared by ZnO-initiated Photopolymerization for La (III) Adsorption. ACS Appl. Mater. Interfaces *6*, 19840–19849. https://doi.org/10.1021/am505177c.

19. Tang, S.C.N., Yan, D.Y.S., and Lo, I.M.C. (2014). Sustainable Wastewater Treatment Using Microsized Magnetic Hydrogel with Magnetic Separation Technology. Ind. Eng. Chem. Res. *53*, 15718–15724. https://doi.org/10.1021/ie502512h.

20. Rahban, D., Doostan, M., and Salimi, A. (2020). Cancer Therapy; Prospects for Application of Nanoparticles for Magnetic-Based Hyperthermia. Cancer Invest. *38*, 507–521. https://doi.org/10.1080/07357907.2020.1817482.

21. Filippi, M., Garello, F., Yasa, O., Kasamkattil, J., Scherberich, A., and Katzschmann, R.K. (2022). Engineered Magnetic Nanocomposites to Modulate Cellular Function. Small *18*, 2104079. https://doi.org/10.1002/smll.202104079.

22. Liu, Z., Liu, J., Cui, X., Wang, X., Zhang, L., and Tang, P. (2020). Recent Advances on Magnetic Sensitive Hydrogels in Tissue Engineering. Front. Chem. *8*, 124.

23. Wei, H., Cui, J., Lin, K., Xie, J., and Wang, X. (2022). Recent advances in smart stimuli-responsive biomaterials for bone therapeutics and regeneration. Bone Res. *10*, 17–19. https://doi.org/10.1038/s41413-021-00180-y.

24. Wu, C., Fan, W., Zhu, Y., Gelinsky, M., Chang, J., Cuniberti, G., Albrecht, V., Friis, T., and Xiao, Y. (2011). Multifunctional magnetic mesoporous bioactive glass scaffolds with a hierarchical pore structure. Acta Biomater. *7*, 3563–3572. https://doi.org/10.1016/j.actbio.2011.06.028.

25. Giustini, A.J., Petryk, A.A., Cassim, S.M., Tate, J.A., Baker, I., and Hoopes, P.J. (2010). Magnetic nanoparticle hyperthermia in cancer treatment. Nano Life *01*, 17–32. https://doi.org/10.1142/S1793984410000067.

26. Guo, H., Lv, R., and Bai, S. (2019). Recent advances on 3D printing graphene-based composites. Nano Materials Science *1*, 101–115. https://doi.org/10.1016/j.nanoms.2019.03.003.

27. Huber, C., Abert, C., Bruckner, F., Groenefeld, M., Schuschnigg, S., Teliban, I., Vogler, C., Wautischer, G., Windl, R., and Suess, D. (2017). 3D Printing of Polymer-Bonded Rare-Earth Magnets With a Variable Magnetic Compound Fraction for a Predefined Stray Field. Sci. Rep. *7*, 9419. https://doi.org/10.1038/s41598-017-09864-0.

28. Gao, B., Yang, Q., Zhao, X., Jin, G., Ma, Y., and Xu, F. (2016). 4D Bioprinting for Biomedical Applications. Trends Biotechnol. *34*, 746–756. https://doi.org/10.1016/j.tibtech.2016.03.004.

29. Chen, Z., Zhao, D., Liu, B., Nian, G., Li, X., Yin, J., Qu, S., and Yang, W. (2019). 3D Printing of Multifunctional Hydrogels. Adv. Funct. Mater. *29*, 1900971. https://doi.org/10.1002/adfm.201900971.

30. Kim, Y., Yuk, H., Zhao, R., Chester, S.A., and Zhao, X. (2018). Printing ferromagnetic domains for untethered fast-transforming soft materials. Nature *558*, 274–279. https://doi.org/10.1038/S41586-018-0185-0.

31. Arias, L.S., Pessan, J.P., Vieira, A.P.M., Lima, T.M.T.d., Delbem, A.C.B., and Monteiro, D.R. (2018). Iron Oxide Nanoparticles for Biomedical Applications: A Perspective on Synthesis, Drugs, Antimicrobial Activity, and Toxicity. Antibiotics (Basel) *7*, 46. https://doi.org/10.3390/antibiotics7020046.

32. Gavilán, H., Simeonidis, K., Myrovali, E., Mazarío, E., Chubykalo-Fesenko, O., Chantrell, R., Balcells, L., Angelakeris, M., Morales, M.P., and Serantes, D. (2021). How size, shape and assembly of magnetic nanoparticles give rise to different hyperthermia scenarios. Nanoscale *13*, 15631–15646. https://doi.org/10.1039/D1NR03484G.

33. Kuhnt, T., Camarero-Espinosa, S., Takhsha Ghahfarokhi, M., Arreguín, M., Cabassi, R., Albertini, F., Nieto, D., Baker, M.B., and Moroni, L. (2022). 4D Printed Shape Morphing Biocompatible Materials Based on Anisotropic Ferromagnetic Nanoparticles. Adv. Funct. Mater. *32*, 2202539. https://doi.org/10.1002/adfm.202202539.

34. Mauney, J.R., Sjostorm, S., Blumberg, J., Horan, R., O'Leary, J.P., Vunjak-Novakovic, G., Volloch, V., and Kaplan, D.L. (2004). Mechanical stimulation promotes osteogenic differentiation of human bone marrow stromal cells on 3-D partially demineralized bone scaffolds in vitro. Calcif. Tissue Int. *74*, 458–468. https://doi.org/10.1007/s00223-003-0104-7.

35. Kang, K.S., Lee, S.-J., Lee, H.S., Moon, W., and Cho, D.-W. (2011). Effects of combined mechanical stimulation on the proliferation and differentiation of pre-osteoblasts. Exp. Mol. Med. *43*, 367–373. https://doi.org/10.3858/emm.2011.43.6.040.

36. Anderson, D.E., and Johnstone, B. (2017). Dynamic Mechanical Compression of Chondrocytes for Tissue Engineering: A Critical Review. Front. Bioeng. Biotechnol. *5*, 76. https://doi.org/10.3389/fbioe.2017.00076.

37. Fahy, N., Alini, M., and Stoddart, M.J. (2018). Mechanical stimulation of mesenchymal stem cells: Implications for cartilage tissue engineering. J. Orthop. Res. *36*, 52–63. https://doi.org/10.1002/jor.23670.

38. Das, S., Pati, F., Choi, Y.J., Rijal, G., Shim, J.H., Kim, S.W., Ray, A.R., Cho, D.W., and Ghosh, S. (2015). Bioprintable, cell-laden silk fibroin-gelatin hydrogel supporting multilineage differentiation of stem cells for fabrication of three-dimensional tissue constructs. Acta Biomater. *11*, 233–246. https://doi.org/10.1016/J.ACTBIO.2014.09.023.

39. Das, S., Pati, F., Chameettachal, S., Pahwa, S., Ray, A.R., Dhara, S., and Ghosh, S. (2013). Enhanced redifferentiation of chondrocytes on microperiodic silk/gelatin scaffolds: Toward tailor-made tissue engineering. Biomacromolecules *14*, 311–321. https://doi.org/10.1021/BM301193T.

40. Zou, S., Fan, S., Oliveira, A.L., Yao, X., Zhang, Y., and Shao, H. (2022). 3D Printed Gelatin Scaffold with Improved Shape Fidelity and Cytocompatibility by Using Antheraea pernyi Silk Fibroin Nanofibers. Adv. Fiber Mater. *4*, 758–773. https://doi.org/10.1007/s42765-022-00135-w.

41. Chakraborty, J., Mu, X., Pramanick, A., Kaplan, D.L., and Ghosh, S. (2022). Recent advances in bioprinting using silk protein-based bioinks. Biomaterials *287*, 121672. https://doi.org/10.1016/j.biomaterials.2022.121672.

42. Chakraborty, J., Fernández-Pérez, J., van Kampen, K.A., Roy, S., Ten Brink, T., Mota, C., Ghosh, S., and Moroni, L. (2023). Development of a biomimetic arch-like 3D bioprinted construct for cartilage regeneration using gelatin methacryloyl and silk fibroin-gelatin bioinks. Biofabrication *15*, 35009. https://doi.org/10.1088/1758-5090/acc68f.

43. Chawla, S., Kumar, A., Admane, P., Bandyopadhyay, A., and Ghosh, S. (2017). Elucidating role of silk-gelatin bioink to recapitulate articular cartilage differentiation in 3D bioprinted constructs. Bioprinting *7*, 1–13. https://doi.org/10.1016/J.BPRINT.2017.05.001.

44. Chakraborty, J., and Ghosh, S. (2020). Cellular Proliferation, Self-Assembly, and Modulation of

Signaling Pathways in Silk Fibroin Gelatin-Based 3D Bioprinted Constructs. ACS Appl. Bio Mater. *3*, 8309–8320. https://doi.org/10.1021/acsabm.0c01252.

45. Karahaliloğlu, Z., Yalçın, E., Demirbilek, M., and Denkbaş, E.B. (2017). Magnetic silk fibroin e-gel scaffolds for bone tissue engineering applications. J. Bioact. Compat Polym. *32*, 596–614. https://doi.org/10.1177/0883911517693635.

46. Shuai, C., Cheng, Y., Yang, W., Feng, P., Yang, Y., He, C., Qi, F., and Peng, S. (2020). Magnetically actuated bone scaffold: Microstructure, cell response and osteogenesis. Compos. B Eng. *192*, 107986. https://doi.org/10.1016/j.compositesb.2020.107986.

47. Hao, S., Zhang, Y., Meng, J., Liu, J., Wen, T., Gu, N., and Xu, H. (2018). Integration of a Superparamagnetic Scaffold and Magnetic Field to Enhance the Wound-Healing Phenotype of Fibroblasts. ACS Appl. Mater. Interfaces *10*, 22913–22923. https://doi.org/10.1021/acsami.8b04149.

48. Chawla, S., Midha, S., Sharma, A., and Ghosh, S. (2018). Silk-Based Bioinks for 3D Bioprinting. Adv. Healthc. Mater. *7*, e1701204. https://doi.org/10.1002/adhm.201701204.

49. Hu, C., Hahn, L., Yang, M., Altmann, A., Stahlhut, P., Groll, J., and Luxenhofer, R. (2021). Improving printability of a thermoresponsive hydrogel biomaterial ink by nanoclay addition. J. Mater. Sci. *56*, 691–705. https://doi.org/10.1007/S10853-020-05190-5/FIGURES/6.

50. Singh, R.K., Patel, K.D., Lee, J.H., Lee, E.-J., Kim, J.-H., Kim, T.-H., and Kim, H.-W. (2014). Potential of Magnetic Nanofiber Scaffolds with Mechanical and Biological Properties Applicable for Bone Regeneration. PLoS One *9*, e91584. https://doi.org/10.1371/journal.pone.0091584.

51. Bañobre-López, M., Piñeiro-Redondo, Y., De Santis, R., Gloria, A., Ambrosio, L., Tampieri, A., Dediu, V., and Rivas, J. (2011). Poly(caprolactone) based magnetic scaffolds for bone tissue engineering. J. Appl. Phys. *109*, 07B313. https://doi.org/10.1063/1.3561149.

52. Tognato, R., Armiento, A.R., Bonfrate, V., Levato, R., Malda, J., Alini, M., Eglin, D., Giancane, G., and Serra, T. (2019). A Stimuli-Responsive Nanocomposite for 3D Anisotropic Cell-Guidance and Magnetic Soft Robotics. Adv. Funct. Mater. *29*, 1804647. https://doi.org/10.1002/adfm.201804647.

53. Matos, A.M., Gonçalves, A.I., El Haj, A.J., and Gomes, M.E. (2020). Magnetic biomaterials and nano-instructive tools as mediators of tendon mechanotransduction. Nanoscale Adv. *2*, 140–148. https://doi.org/10.1039/C9NA00615J.

54. Gloria, A., Russo, T., D'Amora, U., Zeppetelli, S., D'Alessandro, T., Sandri, M., Bañobre-López, M., Piñeiro-Redondo, Y., Uhlarz, M., Tampieri, A., et al. (2013). Magnetic poly(ε-caprolactone)/iron-doped hydroxyapatite nanocomposite substrates for advanced bone tissue engineering. J. R. Soc. Interface *10*, 20120833. https://doi.org/10.1098/rsif.2012.0833.

55. Del Bianco, L., Spizzo, F., Yang, Y., Greco, G., Gatto, M.L., Barucca, G., Pugno, N.M., and Motta, A. (2022). Silk fibroin films with embedded magnetic nanoparticles: evaluation of the magneto-mechanical stimulation effect on osteogenic differentiation of stem cells. Nanoscale *14*, 14558–14574. https://doi.org/10.1039/D2NR03167A.

56. Chouhan, D., Mehrotra, S., Majumder, O., and Mandal, B.B. (2019). Magnetic Actuator Device Assisted Modulation of Cellular Behavior and Tuning of Drug Release on Silk Platform. ACS Biomater. Sci. Eng. *5*, 92–105. https://doi.org/10.1021/acsbiomaterials.8b00240.

57. Agrawal, S.K., Sanabria-Delong, N., Tew, G.N., and Bhatia, S.R. (2008). Nanoparticle-reinforced associative network hydrogels. Langmuir *24*, 13148–13154. https://doi.org/10.1021/la8015518.

58. Coïsson, M., Barrera, G., Celegato, F., Martino, L., Kane, S.N., Raghuvanshi, S., Vinai, F., and Tiberto, P. (2017). Hysteresis losses and specific absorption rate measurements in magnetic nanoparticles for hyperthermia applications. Biochim. Biophys. Acta. Gen. Subj. *1861*, 1545–1558. https://doi.org/10.1016/j.bbagen.2016.12.006.

59. Shah, R.R., Davis, T.P., Glover, A.L., Nikles, D.E., and Brazel, C.S. (2015). Impact of magnetic field parameters and iron oxide nanoparticle properties on heat generation for use in magnetic hyperthermia. J. Magn. Magn Mater. *387*, 96–106. https://doi.org/10.1016/j.jmmm.2015.03.085.

60. Atkinson, W.J., Brezovich, I.A., and Chakraborty, D.P. (1984). Usable frequencies in hyperthermia with thermal seeds. IEEE Trans. Biomed. Eng. *31*, 70–75. https://doi.org/10.1109/TBME.1984.325372.

61. Korson, L., Drost-Hansen, W., and Millero, F.J. (1969). Viscosity of water at various temperatures. J. Phys. Chem. *73*, 34–39. https://doi.org/10.1021/j100721a006.

62. Bi, R., Yin, Q., Mei, J., Chen, K., Luo, X., Fan, Y., and Zhu, S. (2020). Identification of human temporomandibular joint fibrocartilage stem cells with distinct chondrogenic capacity. Osteoarthritis Cartilage *28*, 842–852. https://doi.org/10.1016/j.joca.2020.02.835.

63. Tuan, R.S. (2006). Stemming cartilage degeneration: adult mesenchymal stem cells as a cell source for articular cartilage tissue engineering. Arthritis Rheum. *54*, 3075–3078. https://doi.org/10.1002/art.22148.

64. Seda Tigli, R., Ghosh, S., Laha, M.M., Shevde, N.K., Daheron, L., Gimble, J., Gümüşderelioglu, M., and Kaplan, D.L. (2009). Comparative chondrogenesis of human cell sources in 3D scaffolds. J. Tissue Eng. Regen. Med. *3*, 348–360. https://doi.org/10.1002/term.169.

65. Shi, W., Sun, M., Hu, X., Ren, B., Cheng, J., Li, C., Duan, X., Fu, X., Zhang, J., Chen, H., and Ao, Y. (2017). Structurally and Functionally Optimized Silk-Fibroin-Gelatin Scaffold Using 3D Printing to Repair Cartilage Injury In Vitro and In Vivo. Adv. Mater. *29*. https://doi.org/10.1002/adma.201701089.

66. Singh, Y.P., Bandyopadhyay, A., and Mandal, B.B. (2019). 3D Bioprinting Using Cross-Linker-Free Silk-Gelatin Bioink for Cartilage Tissue Engineering. ACS Appl. Mater. Interfaces *11*, 33684–33696. https://doi.org/10.1021/acsami.9b11644.

67. Varghese, S., Hwang, N.S., Canver, A.C., Theprungsirikul, P., Lin, D.W., and Elisseeff, J. (2008). Chondroitin sulfate based niches for chondrogenic differentiation of mesenchymal stem cells. Matrix Biol. *27*, 12–21. https://doi.org/10.1016/j.matbio.2007.07.002.

68. Huang, D.-M., Hsiao, J.-K., Chen, Y.-C., Chien, L.-Y., Yao, M., Chen, Y.-K., Ko, B.-S., Hsu, S.-C., Tai, L.-A., Cheng, H.-Y., et al. (2009). The promotion of human mesenchymal stem cell proliferation by superparamagnetic iron oxide nanoparticles. Biomaterials *30*, 3645–3651. https://doi.org/10.1016/j.biomaterials.2009.03.032.

69. Hughes, S., El Haj, A.J., and Dobson, J. (2005). Magnetic micro- and nanoparticle mediated activation of mechanosensitive ion channels. Med. Eng. Phys. *27*, 754–762. https://doi.org/10.1016/j.medengphy.2005.04.006.

70. Shen, J.-F., Chao, Y.-L., and Du, L. (2007). Effects of static magnetic fields on the voltage-gated potassium channel currents in trigeminal root ganglion neurons. Neurosci. Lett. *415*, 164–168. https://doi.org/10.1016/j.neulet.2007.01.015.

71. Cámara-Torres, M., Sinha, R., Sanchez, A., Habibovic, P., Patelli, A., Mota, C., and Moroni, L. (2022). Effect of high content nanohydroxyapatite composite scaffolds prepared via melt extrusion additive manufacturing on the osteogenic differentiation of human mesenchymal stromal cells. Biomater. Adv. *137*, 212833. https://doi.org/10.1016/j.bioadv.2022.212833.

72. Chakraborty, J., Majumder, N., Sharma, A., Prasad, S., and Ghosh, S. (2022). 3D bioprinted silk-reinforced Alginate-Gellan Gum constructs for cartilage regeneration. Bioprinting *28*, e00232. https://doi.org/10.1016/j.bprint.2022.e00232.

73. Admane, P., Gupta, A.C., Jois, P., Roy, S., Chandrasekharan Lakshmanan, C., Kalsi, G., Bandyopadhyay, B., and Ghosh, S. (2019). Direct 3D bioprinted full-thickness skin constructs recapitulate regulatory signaling pathways and physiology of human skin. Bioprinting *15*, e00051. https://doi.org/10.1016/J.BPRINT.2019.E00051.

74. Camarero-Espinosa, S., Tomasina, C., Calore, A., and Moroni, L. (2020). Additive manufactured, highly resilient, elastic, and biodegradable poly(ester)urethane scaffolds with chondroinductive properties for cartilage tissue engineering. Mater. Today. Bio *6*, 100051. https://doi.org/10.1016/J.MTBIO.2020.100051.

75. Ignat'eva, N.Y., Danilov, N.A., Averkiev, S.V., Obrezkova, M.V., Lunin, V.V., and Sobol', E.N. (2007). Determination of hydroxyproline in tissues and the evaluation of the collagen content of the tissues. J. Anal. Chem. *62*, 51–57. https://doi.org/10.1134/S106193480701011X.